

# Volatile Organic Compound Detection Using Insect Odorant-Receptor Functionalised Field-Effect Transistors

by

Eddyn Oswald Perkins Treacher

A thesis submitted in fulfilment of the  
requirements of the degree of  
Doctor of Philosophy in Physics  
School of Physical and Chemical Sciences  
Te Herenga Waka - Victoria University of Wellington

Sep 2023





# Acknowledgements

69450

Rifat, Alex - vapour sensor  
Erica Cassie - FET sensing setup  
Rob Keyzers and Jennie Ramirez-Garcia - NMR spectra  
Patricia Hunt - Computational chemistry



# **Abstract**

This is a thesis skeleton written with quarto. Make a copy of this thesis repo and start to write!

Make a new paragraph by leaving a blank line.



# Table of contents

<b>Acknowledgements</b>	<b>1</b>
<b>Abstract</b>	<b>3</b>
<b>1. Introduction</b>	<b>9</b>
<b>2. Carbon Nanotube and Graphene Field-Effect Transistors</b>	<b>11</b>
2.1. Ambipolar Field-Effect Transistors . . . . .	11
2.1.1. Gating . . . . .	11
2.1.2. Electrical Properties . . . . .	11
<b>3. Carbon Nanotube and Graphene Field-Effect Transistors as Biosensor Platforms</b>	<b>13</b>
3.1. Carbon Nanotube Networks & Graphene as Biosensing Transducers . . . . .	13
3.2. Biosensor Examples . . . . .	13
3.2.1. Sensor Types . . . . .	13
3.2.2. Sensor Functionalisation . . . . .	13
3.2.3. Sensing Methods . . . . .	13
3.3. Insect Odorant Receptors . . . . .	13
3.4. Non-Specific Binding . . . . .	13
3.4.1. Non-Specific Binding to Channels . . . . .	13
3.4.2. Non-Specific Binding to Apparatus . . . . .	13
<b>4. Fabrication of Carbon Nanotube Network and Graphene Field-Effect Transistors</b>	<b>15</b>
4.1. Deposition of Carbon Nanotubes . . . . .	15
4.1.1. Solvent-Based . . . . .	16
4.1.2. Surfactant-Based . . . . .	16
4.2. Photolithography for Carbon Nanotube and Graphene Field-Effect Transistors . . . . .	18
4.2.1. Alignment Markers . . . . .	20
4.2.2. Channel Etching . . . . .	20
4.2.3. Electrodes . . . . .	21
4.2.4. Encapsulation . . . . .	23
4.3. Characterisation via Atomic Force Microscopy . . . . .	26
4.4. Characterisation via Fluorescence Microscopy . . . . .	26
4.5. Electrical Characterisation . . . . .	26

*Table of contents*

4.6. Summary . . . . .	29
<b>5. Characteristics of Pristine Carbon Nanotube &amp; Graphene Field Effect Transistors</b>	<b>31</b>
5.1. Carbon Nanotube Network Morphology . . . . .	31
5.2. Salt Concentration Sensing with Phosphate Buffered Saline . . . . .	34
<b>6. Functionalisation of Carbon Nanotubes and Graphene with Odorant Receptors</b>	<b>35</b>
6.1. Linker molecules . . . . .	35
6.1.1. 1-Pyrenebutanoic acid N-hydroxysuccinimide ester (PBASE) . . .	35
6.2. Functionalisation with Odorant Receptors on CNT network . . . . .	39
6.2.1. Varying CNT network fabrication approach . . . . .	39
6.2.2. Varying OR-nanodisc preparation process . . . . .	39
6.2.3. Varying solvent used . . . . .	39
6.2.4. Other functionalisation approaches . . . . .	39
6.3. Functionalisation with Odorant Receptors on graphene . . . . .	39
6.4. Verifying Pyrene Attachment to CNT network and graphene . . . . .	39
6.4.1. Photoresist contamination . . . . .	39
6.4.2. Raman Spectroscopy . . . . .	39
6.4.3. Pyrene-PEG-FITC fluorescence microscopy . . . . .	39
6.4.4. Pyrene-PEG electrical characterisation . . . . .	39
<b>7. Vapour Phase Sensing with Transistor Biosensors</b>	<b>41</b>
7.1. Testing Vapour Delivery System . . . . .	41
7.1.1. System Description . . . . .	41
7.1.2. Temperature and Humidity Indicator . . . . .	41
7.1.3. Photoionisation Detector . . . . .	41
<b>8. Summary</b>	<b>43</b>
<b>Appendices</b>	<b>43</b>
<b>A. Photolithography</b>	<b>45</b>
A.1. AZ® 1518 photoresist . . . . .	47
A.2. AZ® nLOF 2020 photoresist . . . . .	47
A.3. SU8-2150 photoresist . . . . .	48
<b>B. Python Code for Data Analysis</b>	<b>49</b>
B.1. Code Repository . . . . .	49
B.2. Atomic Force Microscope Histogram Analysis . . . . .	49
<b>C. Vapour Delivery System</b>	<b>51</b>
C.1. Technical Notes . . . . .	51

*Table of contents*

C.2. Future Improvements . . . . .	51
------------------------------------	----



# 1. Introduction

This is a book created from markdown and executable code.

See for additional discussion of literate programming.

[1] 2



## **2. Carbon Nanotube and Graphene Field-Effect Transistors**

### **2.1. Ambipolar Field-Effect Transistors**

#### **2.1.1. Gating**

Back-gating

Liquid-gating

#### **2.1.2. Electrical Properties**



### **3. Carbon Nanotube and Graphene Field-Effect Transistors as Biosensor Platforms**

#### **3.1. Carbon Nanotube Networks & Graphene as Biosensing Transducers**

#### **3.2. Biosensor Examples**

##### **3.2.1. Sensor Types**

##### **3.2.2. Sensor Functionalisation**

##### **3.2.3. Sensing Methods**

Aqueous Environment

Vapour Environment

#### **3.3. Insect Odorant Receptors**

#### **3.4. Non-Specific Binding**

##### **3.4.1. Non-Specific Binding to Channels**

##### **3.4.2. Non-Specific Binding to Apparatus**

Encapsulation

PDMS Well

Reference Electrode



## 4. Fabrication of Carbon Nanotube Network and Graphene Field-Effect Transistors

This chapter discusses the fabrication processes for both the carbon nanotube network and graphene transistors. Experimental optimisation of the transducer element is critical for biosensor work, and large numbers of transducers were required for testing various biosensor functionalisation processes. Therefore, these processes were developed to rapidly fabricate devices with reproducible device characteristics appropriate for biosensing work. Also outlined in this chapter are the characterisation techniques taken to test the quality and reproducibility of these fabrication processes.

The nitrogen ( $\geq 99.99\%$ ) and oxygen (99.7%) used in fabrication work was supplied by BOC Limited New Zealand. All acetone and isopropanol used for wafer/device processing had a minimum 99.9% purity (HPLC grade). Deionised (DI) water was taken from a Synergy<sup>®</sup> UV Water Purification System. The DI water had a measured conductivity of  $(1.4 \pm 0.1) \mu\text{S cm}^{-1}$ , compared to tap water with a measured conductivity of  $(7.8 \pm 0.2) \mu\text{S cm}^{-1}$ .

### 4.1. Deposition of Carbon Nanotubes

4-inch *p*-type (B-doped) silicon wafers with either a 100 nm or 300 nm SiO<sub>2</sub> layer (Wafer-Pro LLC) were used as the substrate for carbon nanotube network deposition. A 100 nm SiO<sub>2</sub> layer was the preferred option for the devices intended for backgated measurements. Before deposition of carbon nanotubes, the wafers were spin-coated with AZ<sup>®</sup> 1518 photoresist, placed photoresist-side down onto a cleanroom wipe, fixed in place using vacuum suction, then cleaved into quarters using a diamond-tipped scribe tool.

For fabrication performed before June 2023, the protective photoresist layer was then removed by soaking the quarter-wafers in acetone for 15 minutes, then rinsed with isopropyl alcohol (IPA) and dried with N<sub>2</sub> gas. However, for complete removal of photoresist, we found it was necessary to flood expose the wafer with the Karl Suss Aligner for 1 min and then place it in AZ326 developer for 3 min, as discussed further in Section 6.4.1.

Carbon nanotubes were deposited before alignment markers photolithography on all wafers fabricated between Aug 2021-Feb 2023, while devices fabricated before Aug 2021

#### *4. Fabrication of Carbon Nanotube Network and Graphene Field-Effect Transistors*

and after Feb 2023 had alignment markers photolithography performed before the deposition of carbon nanotubes. The process order was first switched in Aug 2021 as this order led to faster processing times. However, the order was switched back in Feb 2023 to minimise the exposure of carbon nanotubes to photolithographic chemical processes.

##### **4.1.1. Solvent-Based**

The solvent-based deposition process for the carbon nanotube network in the second fabrication protocol is as follows. 10 mg of 2-mercaptopurine (99%, Sigma-Aldrich) was dissolved in 1 ml ethanol by sonication until clear. Quarter wafers were sonicated in acetone for 3 min, then exposed to O<sub>2</sub> plasma at 100 W for at least 2 min in a small plasma cleaner (Plasma Etch, Inc., PE-50 Compact Benchtop Plasma Cleaning System) or reactive ion etcher (Oxford Instruments, Plasmalab® 80 Plus) under 300 mTorr pressure. The cleaned SiO<sub>2</sub>/Si surface was then coated with 2-mercaptopurine for 10 minutes, rinsed with ethanol to remove residual 2-mercaptopurine, and then nitrogen dried.

Meanwhile, 5 μ g of 99% semiconducting carbon nanotube bucky paper (NanoIntegris, IsoNanotubes S-99) was dispersed in 10 mL of anhydrous 1,2-dichlorobenzene (Sigma Aldrich) by ultrasonication until no particles were visible to the naked eye. During this time, the ultrasonic bath temperature was kept between 20 - 30 °C or the buckypaper would not disperse successfully. The substrates were then placed into a dish with CNT-DCB suspension and left covered for 1 hour, dipped into ethanol for 10 min to remove residual solvent and any unattached carbon nanotube bundles, and then dried with nitrogen.

##### **4.1.2. Surfactant-Based**

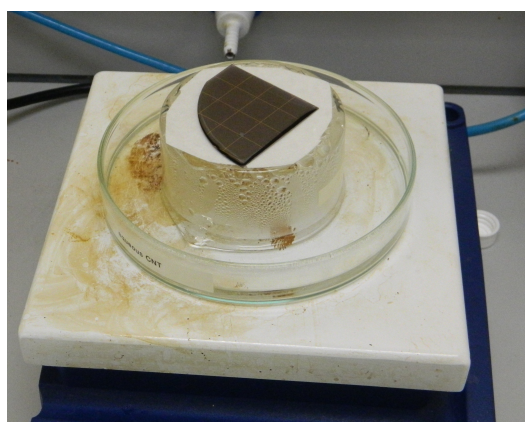
Two different approaches were used to attach the surfactant-dispersed CNTs. In both approaches, the quarter wafers were rinsed with ultrapure deionised water (DI water), acetone and IPA before being placed into a reactive ion etcher (Oxford Instruments, Plasmalab 80 Plus) and exposed to O<sub>2</sub> plasma at 100 W for at least 2 min in a small plasma cleaner (Plasma Etch, Inc, PE-50 Compact Benchtop Plasma Cleaning System) or reactive ion etcher (Oxford Instruments, Plasmalab 80 Plus) under 300 mTorr pressure to make the surface hydrophilic. 1 mL of poly-L-lysine (PLL) was immediately deposited onto each quarter wafer and left for 5 minutes. The quarter wafers were then rinsed for 30 s with DI water and dried with N<sub>2</sub> gas. This process allows for the surface adhesion of semiconducting single carbon nanotubes suspended in surfactant.

#### 4.1. Deposition of Carbon Nanotubes

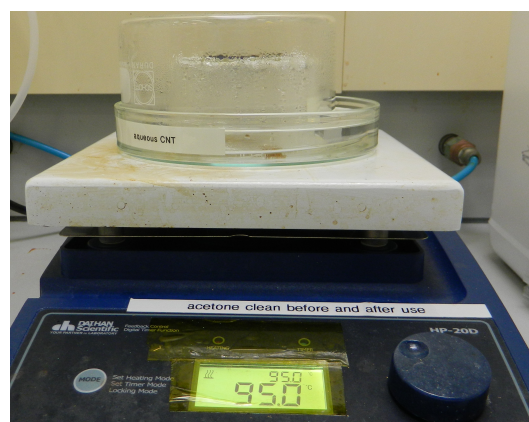
##### Simple Dropcasting

2 mL of IsoNanotubes-S 90% or 99% solution (NanoIntegris) was decanted into a small bottle and sonicated for 5 s to break up bundles of CNTs. An even spread of 400  $\mu$ L CNT solution was placed in the centre of the PLL-functionalised quarter wafer, covered and left for 10 minutes. The CNT solution was then rinsed off with DI water and IPA, and then the quarter wafer was dried with N<sub>2</sub> gas. Next, the quarter wafer was annealed in a vacuum oven at 150° C for 1 hour. This method would often lead to an inhomogeneous spread of CNTs across the quarter wafer surface, detailed further in section Section 6.2.1.

##### Steam-Assisted Method



(a) Steam method setup without steam cover



(b) Steam method setup with steam cover

Figure 4.1.: Photographs of steam-assisted method setup (top and side view).

2 mL of IsoNanotubes-S 90% or 99% solution (NanoIntegris) was decanted into a small bottle and burst-sonicated once (on then off again) to break up bundles of CNTs. 75 mL of 95° C water was then placed into a glass dish on a hotplate held at 95° C. After this, the PLL-functionalised quarter wafer was placed in the centre of an insulating surface on the same hotplate. The CNT dispersion was carefully spread across the surface of the wafer without spilling any over the wafer edges. The wafer on the insulating surface and glass dish were then left under the same cover for 2 minutes to expose the wafer to steam from the glass dish. The use of an insulating surface meant that the wafer and CNT dispersion were not heated from below while exposed to steam. The steam-assisted deposition setup is shown in Figure 4.1.

The CNT dispersion was then rinsed off the wafer with DI water, ethanol, acetone and IPA, and then the quarter wafer was dried with N<sub>2</sub> gas. As in the original method, the quarter wafer was then annealed in a vacuum oven at 150° C for 1 hour. This method gave an even spread of CNTs across the quarter wafer surface, leading to a

#### 4. Fabrication of Carbon Nanotube Network and Graphene Field-Effect Transistors

greater consistency in performance between devices. Further details can be found in Section 6.2.1.

### 4.2. Photolithography for Carbon Nanotube and Graphene Field-Effect Transistors

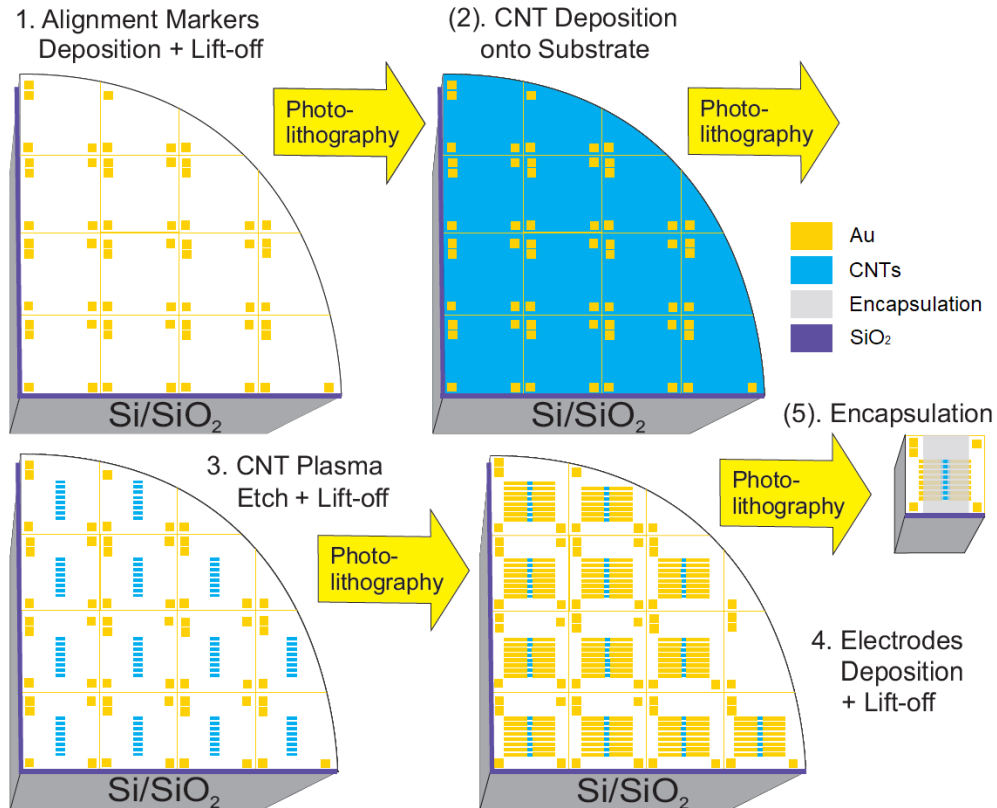


Figure 4.2.: The photolithographic processes used for fabrication of both carbon nanotube and graphene devices (graphene devices were fabricated individually for every step, step #2 skipped for graphene devices)

Photolithography was used to define eight channel regions on each device and subsequently to define metal contacts for each of these channels. A schematic demonstrating these photolithography processes on a quarter wafer is shown in Figure 4.2. Masks for photolithography were designed in-house using LayoutEditor CAD software and patterned externally with a UV laser writer.

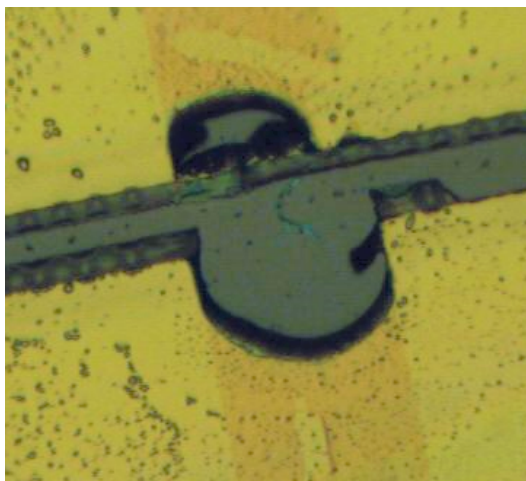
Thermal evaporation was used when depositing chromium (Cr-plated tungsten rods, Kurt J. Lesker) and gold (Au wire, 99.99%, Regal Castings Ltd.), while electron beam evaporation was used when depositing titanium (Ti pieces, 99.99%, Kurt J. Lesker) and

#### 4.2. Photolithography for Carbon Nanotube and Graphene Field-Effect Transistors

metal oxides (*e.g.* Al<sub>2</sub>O<sub>3</sub> pieces, 99.99%, Kurt J. Lesker). Metal and metal oxide deposition was performed using an Angstrom Engineering Nexdep 200 Vacuum Deposition System. Deposition thickness was controlled using an Inficon Deposition Controller and electron beam power was provided by a Telemark TT-6 power supply. For metals, the chamber was initially evacuated to a pressure  $5 \times 10^{-6}$  mTorr, while for metal oxides the chamber was initially evacuated to a pressure of  $1 \times 10^{-5}$  mTorr. After evaporation, the chamber was cooled and vented with nitrogen.

Carbon nanotube devices were fabricated using the quarter wafer substrates discussed in Section 4.1.

Graphene devices were fabricated using 300 nm SiO<sub>2</sub>/p-type Si substrates covered with a monolayer of mechanically transferred CVD graphene (Advanced Chemical Supplier). This substrate was cleaved into equal-sized square chips before photolithography, with side length between 11.6 - 11.7 mm, subject to variability in wafer size. The same cleaving process outlined in Section 4.1 was used for cleaving the chips, but the photoresist was not rinsed off after cleaving. Devices were exposed to a brief burst of N<sub>2</sub> gas to remove any dust from the cleaving process from the surface of devices. When not being used in photolithography, devices were stored in a vacuum desiccator to prevent the quality of the graphene deteriorating with exposure to air over time.



(a) Damage to gold electrode in channel region after DMSO lift-off



(b) Damage to graphene (blue region) after DMSO lift-off

Figure 4.3.: Lift-off with dimethyl sulfoxide sometimes led to damage to regions where nanomaterials were present.

Dimethyl sulfoxide (DMSO) was sometimes used in lift-off processes instead of acetone between Jul 2021 and Feb 2023 because of its effectiveness as a photoresist stripping agent. However, it was abandoned due to some indications it was too aggressive for the devices being fabricated, as shown in Figure 4.3 and also as detailed in Section 6.2.1. It is possible that heat from the electrodes deposition sometimes crosslinked residual

#### *4. Fabrication of Carbon Nanotube Network and Graphene Field-Effect Transistors*

photoresist on the nanomaterial, and then during lift-off was removed aggressively together with any attached nanomaterial by the DMSO. However, it is also possible that prolonged exposure to DMSO alone was sufficient to detach nanomaterial from the substrate. Therefore, acetone was the preferred agent for lift-off despite being a less efficient stripping agent than DMSO.

From Jul 2023 onwards, after each photolithography step using negative resist, quarter wafers/chips placed in AZ326 or SU8 developer for 3 min to ensure complete removal of photoresist residue. For each step with positive resist, the same procedure was performed but with a flood exposure with UV light for 1 min before being placed in developer. The exception to this rule was for devices with an aluminium oxide layer present. Tetramethylammonium hydroxide (TMAH), the active ingredient of AZ® 326, etches through aluminium oxide and causes electrical shorts through the dielectric layer [1], [2]. A further discussion showing the results of this process is given in Section 6.4.1.

##### **4.2.1. Alignment Markers**

Metal alignment markers were deposited in order to accurately align the device channels with device electrodes in subsequent photolithography steps. These alignment markers were asymmetric to indicate the orientation of the device for subsequent photolithography steps and electrical characterisation. In later discussion, channel 1 is defined as the channel placed closest to the large, double square alignment marker.

For carbon nanotube quarter wafers, alignment markers were deposited either directly before or after carbon nanotube deposition (see Section 4.1 for discussion). For graphene devices, alignment markers were deposited directly after cleaving using the protective photoresist layer spincoated prior to cleaving. AZ® 1518 was used for alignment marker photolithography.

For carbon nanotube devices made before Jun 2022, chromium was used as an adhesive layer for gold, while for all graphene devices and carbon nanotube devices made after Jun 2022, titanium was used as the adhesive layer. For chromium/gold depositions, a nominal 10 nm of chromium was deposited followed by a nominal 100 nm Au layer. For titanium/gold depositions, a nominal 10-20 nm of titanium was deposited followed by a nominal 50 nm Au layer (for independent measurements of metal layer thickness, see Section 4.2.3). Devices were then soaked in acetone for at least 2 hours for photoresist lift-off, washed in IPA and dried with nitrogen. The use of titanium gave rise to a cleaner lift-off and improved gold adhesion. Using a relatively thin gold layer (50 nm nominal instead of 100 nm) proved to still be clearly visible but to a cleaner lift-off.

##### **4.2.2. Channel Etching**

Eight channel features, each 1000  $\mu\text{m}$  in length and 100  $\mu\text{m}$  in width with a pitch of 1200  $\mu\text{m}$ , were patterned using AZ® 1518 photolithography on each carbon nanotube or

## 4.2. Photolithography for Carbon Nanotube and Graphene Field-Effect Transistors

graphene-covered substrate. Unwanted nanomaterial not covered with photoresist was then etched away with 200 W oxygen plasma at 600 mTorr using a reactive ion etcher or RIE (Plasmalab® 80 Plus, Oxford Instruments). The etch time was 3 minutes for carbon nanotube quarter wafers, and 1 minute for graphene chips. The protective photoresist was then removed by soaking in acetone for at least 5 minutes.

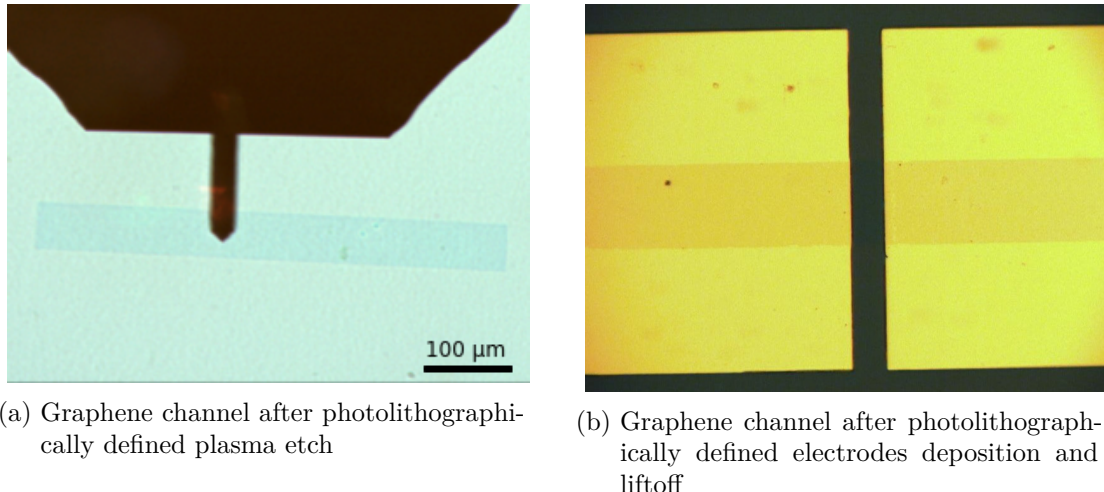


Figure 4.4.: Microscope images of a graphene channel after plasma etch and electrodes photolithography steps.

### 4.2.3. Electrodes

The source and drain electrodes for each channel were patterned using photolithography with either AZ® 1518 photoresist (pre-Mar 2023) or AZ® nLOF 2020 photoresist (post-Mar 2023). Before metal deposition, the developed photoresist pattern was exposed to O<sub>2</sub> plasma at 50 W for up to 5 s or at 20 W for 20-25 s in a PE-50 plasma cleaner (Plasma Etch, Inc.) to remove residual photoresist on the developed regions and ensure a clean lift-off. After metal deposition, wafers/devices were soaked in acetone for at least 2 hours for photoresist lift-off, washed in IPA and dried with nitrogen.

As with the alignment markers deposition (see Section 4.2.1), before Jun 2022 chromium was used for the gold adhesion layer, and after Jun 2022 titanium was used. Adhesion layers are required to stick metals such as gold and platinum to silicon dioxide [3]. A 20 nm nominal titanium layer instead of 10 nm nominal was found to give better electrode adhesion, and devices after Feb 2023 were made using this thicker adhesion layer. Good electronic contact could be made with electrodes with a nominal gold layer thickness of 60-100 nm, and a Au layer nominally 100 nm thick was most commonly used.

Example height profiles of chromium layer channels and a titanium layer channels taken using a Veeco Dektat 150 profiler are shown in Figure 4.5a. AZ® 1518 photoresist was

#### 4. Fabrication of Carbon Nanotube Network and Graphene Field-Effect Transistors

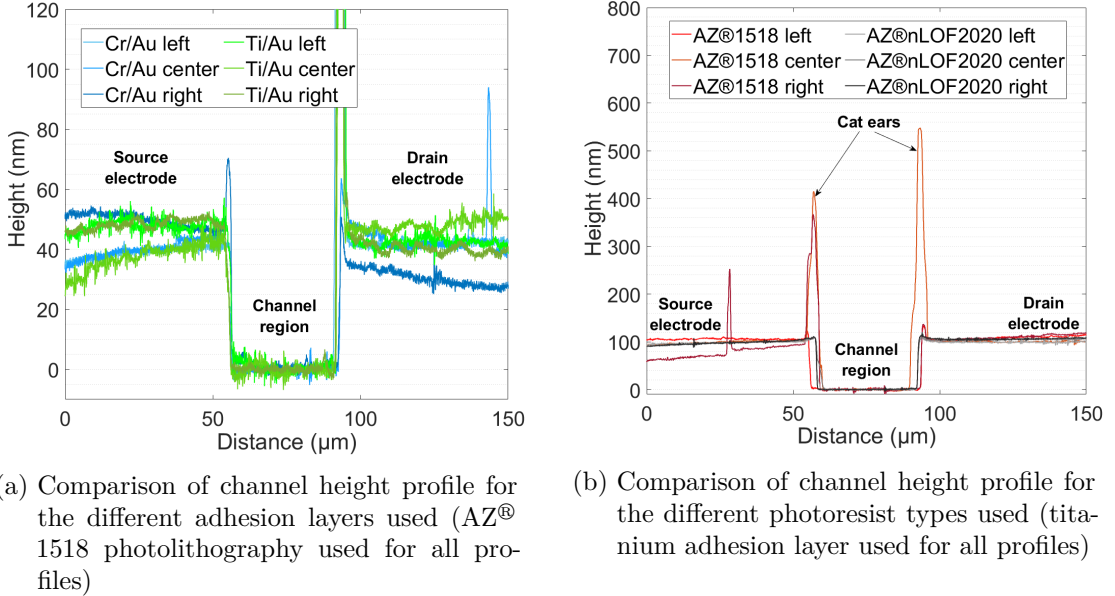


Figure 4.5.: Dektat height profiles taken between the source and drain electrodes across a channel from various quarter wafers with electrodes deposited using different approaches. For each quarter wafer, the profiles of three different channels are shown, selected from different locations across the quarter wafer surface.

used here for photolithographic patterning. A 10 nm adhesion layer and 100 nm Au layer were used for both depositions to ensure a consistent comparison. From Figure 4.5a, we find measured Cr/Au electrode height of  $42 \pm 1$  nm and an measured Ti/Au electrode height of  $48 \pm 2$  nm, slightly less than half the respective heights stated on the Inficon Deposition Controller.

Although using AZ® nLOF 2020 photolithography involves more processing steps, it gave rise to more cleanly-defined electrodes with a more consistent height profile. Often electrodes deposition using AZ® 1518 photoresist would lead to sharp vertical spikes along the edge of the electrode. These edge spikes or “cat ears” could partially or fully protrude through thin encapsulation materials such as SU8 and Al<sub>2</sub>O<sub>3</sub>, leading to significant leakage currents from the electrodes into the FET top gate. This effect is due to the profile of positive resists being suboptimal for lift-off processes, as discussed in Appendix A.

The height profiles corresponding to a wafer with electrodes fabricated using AZ® 1518 and to a wafer with electrodes fabricated using AZ® nLOF 2020 are shown in Figure 4.5b. A 20 nm titanium adhesion layer and 100 nm Au layer were used for both depositions to ensure a consistent comparison, resulting in a measured electrode height of  $103 \pm 2$  nm for both wafers. The wafer which used AZ® nLOF 2020 photoresist clearly has a more consistent electrode height profile across the wafer surface than the wafer which used AZ® 1518 resist. The measured edge features for the AZ® 1518 resist electrodes

## 4.2. Photolithography for Carbon Nanotube and Graphene Field-Effect Transistors

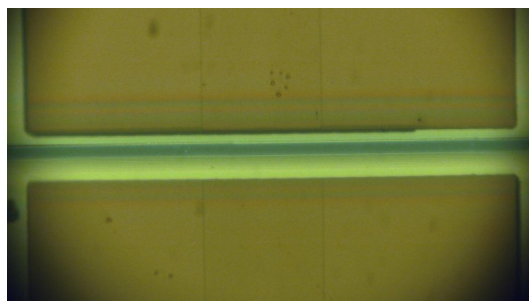
vary in size from 20 nm to 450 nm above the bulk electrode surface, whereas the edge features for the AZ® nLOF 2020 resist do not exceed 14 nm in height.

### 4.2.4. Encapsulation

Several different approaches were used for the encapsulation, or contact protection, of devices. The encapsulation of graphene and carbon-nanotube transistors for biosensing is essential to improve transistor characteristics, passivate the electrodes and ensure only the nanomaterial region is active during biosensing, as discussed in Section 3.2.3.

Before encapsulation photolithography the carbon-nanotube network quarter wafers were cleaved into individual 11 mm x 11 mm chips, using the cleaving process outlined in Section 4.1. Cleaving the devices at this step simplified mask alignment and ensured consistent thickness across photoresist encapsulated devices.

Two different photolithography masks were used for encapsulation photolithography in this work, with different exposed areas of active nanomaterial. The first mask was used for devices made before Jan 2023, and was designed to leave a region of 500  $\mu\text{m}$  x 10  $\mu\text{m}$  unencapsulated for each channel. The second mask was used exclusively after Jan 2023, and was designed to leave a region of 200  $\mu\text{m}$  x 20  $\mu\text{m}$  unencapsulated for each channel. This change was made to double the area of carbon nanotubes exposed to electrolyte while halving the area of SiO<sub>2</sub> dielectric exposed to electrolyte during aqueous sensing.



(a) Encapsulation with AZ® 1518 using pre-2023 mask



(b) Encapsulation with AZ® 1518 using 2023 mask

Figure 4.6.: Microscope images of carbon nanotube devices after encapsulation photolithography with hardbaked AZ® 1518.

A side-by-side microscope comparison of hardbaked AZ® 1518 processed with each mask is given in Figure 4.6, while a Dektat profile comparison corresponding to Figure 4.6 is shown in Figure 4.7a. The profiles corresponding to the mask used after Jan 2023 clearly exhibit greater device-to-device consistency, partly due to the mask requiring a greater level of accuracy when aligning the encapsulation pattern with the electrode channel. The larger feature size also means development time has less of an impact on the quality of the encapsulation opening.

#### 4. Fabrication of Carbon Nanotube Network and Graphene Field-Effect Transistors

##### Photoresist encapsulation

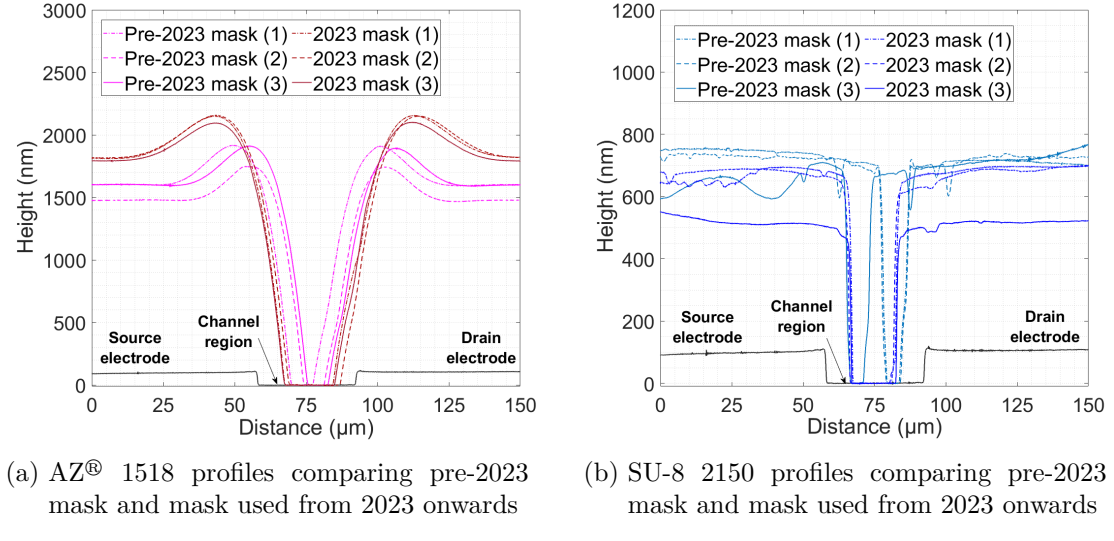


Figure 4.7.: Dektat of carbon nanotube devices after encapsulation photolithography using hardbaked AZ® 1518 and SU-8 2150, taken from various devices.

Two types of photoresist were initially trialled for encapsulation, AZ® 1518 and SU-8 2150. Both AZ® 1518 [4]–[6] and SU-8 have been previously used for device encapsulation, with SU-8 noted for being particularly stable and biocompatible [7]–[9]. Once developed, the photoresist pattern was exposed to O<sub>2</sub> plasma at 50 W for up to 5 s or at 20 W for 20–25 s to remove excess photoresist from the encapsulation opening. Devices were then hardbaked at 200°C for 1 hour to fully crosslink the encapsulation layer. This crosslinking ensured subsequent device exposure to solvent did not remove the photoresist encapsulation.

The exposed region clear of AZ® 1518 resist was  $6.8 \pm 0.3 \mu\text{m}$  in width when using the old, pre-2023 mask, while the exposed region was  $16.6 \pm 0.4 \mu\text{m}$  when using AZ® 1518 with the new mask from 2023, as seen in Figure 4.7a. However, the exposed region was reduced for the SU-8 encapsulation relative to the AZ® 1518, with a width of only  $3.6 \pm 0.5 \mu\text{m}$  for the pre-2023 mask, as seen in Figure 4.7b. Photoresist development using SU-8 was significantly more time-sensitive than for the AZ® 1518. This meant when the development time was increased to create a wider encapsulation opening, it was difficult to avoid removing large areas of photoresist across the surface of the encapsulation. This meant using the new mask from 2023 was especially important for maximising the exposed channel region of SU-8 devices. Using the new mask from 2023 with the SU-8 resist gave a significantly improved width of  $13.8 \pm 1.0 \mu\text{m}$  for the exposed region.

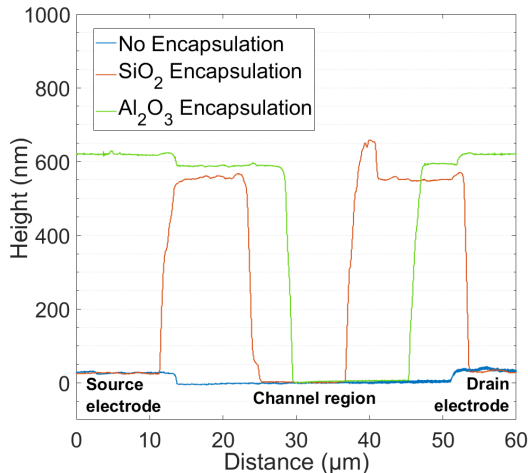
A relatively thin SU-8 encapsulation layer could be deposited when compared to the AZ® 1518 encapsulation profile. The AZ® 1518 encapsulation layer had a average height of  $1.7 \pm 0.2 \mu\text{m}$ , while the SU-8 encapsulation layer had a average height of  $680 \pm 20 \text{ nm}$ .

#### 4.2. Photolithography for Carbon Nanotube and Graphene Field-Effect Transistors

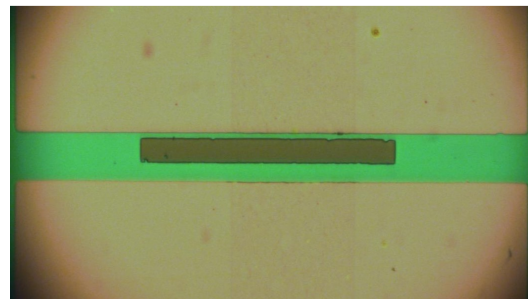
The SU-8 also had much less significant edge features than the AZ® 1518, regardless of the profiles of the source and drain electrodes.

As noted previously, for both resists the overall profile was more consistent for the new, 2023 mask from device to device than for the old pre-2023 mask.

#### Dielectric encapsulation



(a) Profile comparison of dielectric materials used for encapsulation



(b) Microscope image of channel with aluminium oxide encapsulation

Figure 4.8.: Dektat and microscope image of a device encapsulated with aluminium oxide.

Another approach taken was encapsulation of electrode channels with a dielectric metal oxide/ceramic layer. A electron beam deposition process was used to deposit a 100-150 nm nominal metal oxide layer on devices patterned with the 2023 mask using AZ® nLOF 2020 photoresist. As in Section 4.2.3, the developed photoresist pattern was exposed to O<sub>2</sub> plasma at 50 W for up to 5 s or at 20 W for 20-25 s in a PE-50 plasma cleaner (Plasma Etch, Inc.) before ceramic deposition. Before May 2023, devices were left in TechniStrip® MLO 07 (MicroChemicals) for 5-10 min for lift-off. However, due to concerns over the impact of the constituent chemical DMSO on the nanomaterial region (see Figure 4.3), the lift-off process was altered from May 2023 onwards. After May 2023, devices were soaked in acetone for at least 4 hours and sonicated in clean acetone for 30-60 s to lift-off the photoresist, then washed in IPA and dried with nitrogen.

The initial attempt at fabricating a dielectric encapsulation layer used silicon dioxide as the dielectric. However, silicon dioxide adheres poorly to gold without an metallic adhesive layer present, as shown in Figure 4.8a. Aluminium oxide was chosen as an alternative as it sticks well to bulk electrode materials, is heat and chemical resistant, has a relatively high dielectric constant and is bio-compatible [3], [9], [10]. Figure 4.8

#### *4. Fabrication of Carbon Nanotube Network and Graphene Field-Effect Transistors*

shows the aluminium oxide successfully adhered to the electrodes and had a clean profile comparable to that of the SU-8 encapsulation layer after lift-off. As noted earlier, aluminium oxide should not be subsequently exposed to its etchant TMAH.

### **4.3. Characterisation via Atomic Force Microscopy**

Atomic force microscopy in this thesis was taken using a Nanosurf NaioAFM in dynamic force mode. Atomic force microscope (AFM) images could not be taken from the small exposed channel region on the encapsulated devices, so were instead taken on a representative carbon nanotube or graphene film sample fabricated on the same wafer as the device being tested. Moisture adversely affected the AFM imaging process. Therefore, films functionalised with biological materials were washed with DI water and gently dried with N<sub>2</sub> before atomic force microscope images were taken. The open source data analysis software Gwyddion (version 2.59) was used to analyse AFM images.

### **4.4. Characterisation via Fluorescence Microscopy**

Fluorescence microscopy was taken using an Olympus BX63 fluorescence microscope controlled using cellSens imaging software. Microscope objectives used were all Olympus UPLSAPO/UPlanSApo, apochromat objectives which compensate for spherical and chromatic aberrations. Objectives had infinite aperture and a field number of 26.5. Filter cubes used included the Olympus FITC filter (excitation wavelength range: 467-498 nm, emission wavelength range: 513-556 nm), Texas Red (excitation wavelength range: 542-582 nm, emission wavelength range: 604-644 nm) and GFP (excitation wavelength range: 604-644 nm, emission wavelength range: 502-538 nm). The ISO was kept at the lowest available setting, ISO200. All microscopy was performed in darkness with the screen turned away from the microscope. To ensure photobleaching did not adversely affect imaging, images were taken soon after initial exposure to fluorescence and taking repeated photos of the same region was avoided. Various useful and thorough introductions to fluorescence microscopy can be found online [11], [12].

### **4.5. Electrical Characterisation**

Both back-gated and liquid-gated measurements were taken of carbon nanotube and graphene devices. Liquid-gated measurements were taken using the configuration shown in Figure 4.9. Back-gated measurements were taken with a copper plane placed underneath the Si/SiO<sub>2</sub> wafer and connected to SMU 3 instead of the reference electrode.

All measurement setups used had the same basic configuration, with two source measure units (SMUs) attached to the source and gate. Voltage from the source and gate

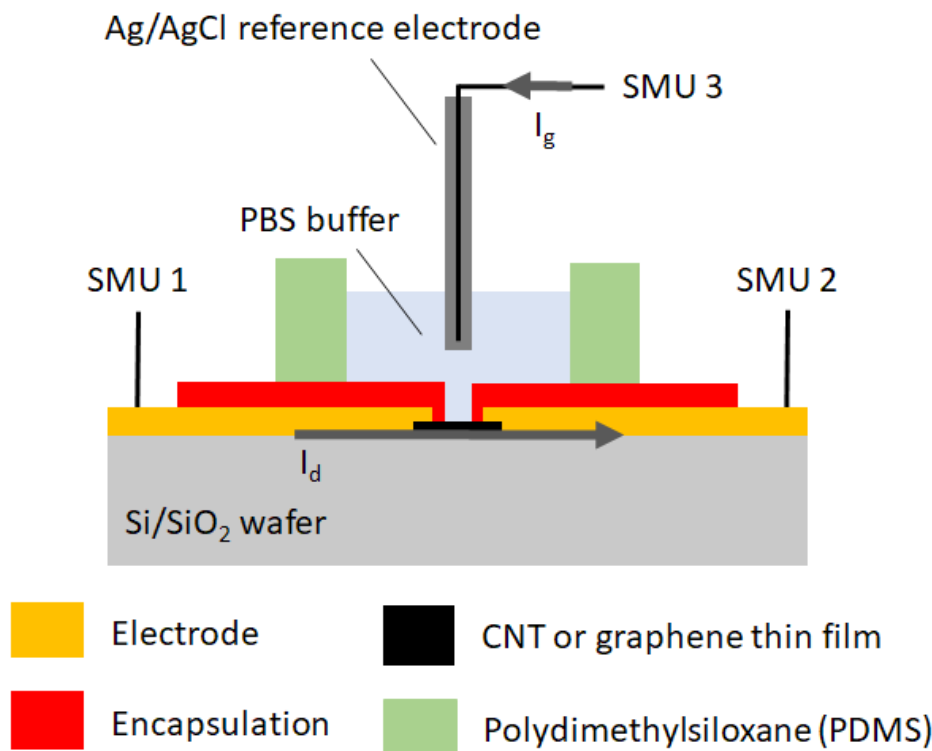
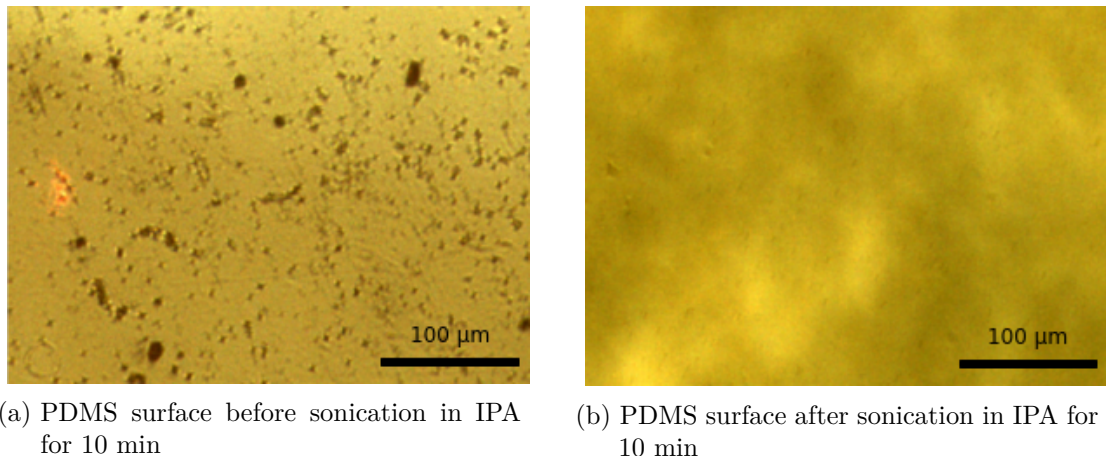


Figure 4.9.: Liquid-gated device schematic showing electrical connections to the three source measure units.  $V_{ds}$  is applied between the source SMU (SMU 1) and the drain SMU (SMU 2), while  $V_{lg}$  is applied between the gate SMU (SMU 3) and the drain SMU. The drain SMU is held at 0 V or connected to a ground plane. Drain current  $I_d$  is measured at the drain SMU, and gate leakage current  $I_g$  is measured at the gate SMU.

#### 4. Fabrication of Carbon Nanotube Network and Graphene Field-Effect Transistors

SMUs was either kept constant or varied, with only one SMU varied at a time. Three different measurement setups were used for taking these measurements, the Keysight (Agilent/HP) 4156C Semiconductor Parameter Analyser, the Keysight B1500A Semiconductor Device Analyser, and a National Instruments NI-PXIe modular measurement system with a 8 GB PXIE-8821 controller and two NI-4138 source measure units. For measurements with the Keysight instruments, a third, drain SMU was attached and kept at a constant 0 V (as shown in Figure 4.9).



(a) PDMS surface before sonication in IPA for 10 min      (b) PDMS surface after sonication in IPA for 10 min

Figure 4.10.: Polydimethylsiloxane (PDMS) surface before and after isopropanol (IPA) sonication for 10 minutes.

When using the Keysight 4156C Semiconductor Parameter Analyser or Keysight B1500A Semiconductor Device Analyser for liquid-gated measurements, a Rucker and Kolls with micromanipulators was used to contact the devices; when using the National Instruments NI-PXIe for liquid-gated measurements, a custom-made chip carrier with spring-loaded, pointed-tip, gold-coated pogo pins was used. Ag/AgCl standard electrodes were used as the liquid-gate electrode. The electrode was submerged in 80  $\mu\text{L}$  of PBS buffer in a polydimethylsiloxane (PDMS) well with outer dimensions of 12 mm x 6 mm x 6 mm. This PDMS well was sonicated in isopropanol for 10 min and thoroughly  $\text{N}_2$  dried before use. The microscope images seen in Figure 4.10 show the PDMS surface before and after this cleaning step. The end of Ag/AgCl standard electrode to be submerged should be rinsed in DI water and left to sit in DI water for 15 minutes before sensing is performed.

The Keysight 4156C Semiconductor Parameter Analyser and Keysight B1500A Semiconductor Device Analyser were also used for back-gated measurements of devices within the vapour delivery system device chamber. This chamber acted as a Faraday cage for another custom-made chip carrier with spring-loaded gold-coated pogo pins.

Custom programs for National Instruments LabView 2017 were used for measurements from the Keysight 4156C Semiconductor Parameter Analyser and the National Instruments NI-PXIe. Keysight EasyEXPERT software was used for characterisation with the Keysight B1500A Semiconductor Device Analyser.

#### 4.6. Summary

Liquid-gated transfer characteristics of carbon nanotube FETs were measured at  $V_{ds} = 100$  mV and liquid-gated transfer characteristics of graphene FETs were measured at  $V_{ds} = 1$  V, where  $V_{lg}$  was swept between -0.5 V and 1 V in both the forward and reverse direction with a step size of 10 mV. Backgated transfer characteristics of carbon nanotube FETs were either measured at  $V_{ds} = 100$  mV or  $V_{ds} = 1$  V, where  $V_{bg}$  was swept between -5 V and 5 V in the forward and reverse directions with a step size of 50 mV.

Sensing measurements were performed with constant source-drain and gate voltages. The gate voltage used was chosen by locating the subthreshold region of the device transfer characteristics and choosing a voltage that fell within this region, usually  $V_g = 0$  V. The choice of gate voltage for sensing measurements is discussed further in Section 3.1 and Section 5.2. Using the NI-PXIe with the PXIe-2737 module, eight-channel multiplexed current measurements could be taken in rapid succession. An integration time of 200 or 400 ms was used for sampling with each channel, with the actual sampling rate set by the NI-PXIe. In practice this meant a sampling rate of 1.81 s (for 200 ms integration time) or 3.41 s (for 400 ms integration time) for any given channel. A 200 ms integration time meant the time between samples from successive channels varied between 220 ms - 230 ms, while a 400 ms integration time meant the time between samples stayed at 426 ms. The other Keysight equipment used a 1 s sampling interval.

## 4.6. Summary

A variety of approaches were trialled when depositing a carbon nanotube network for the fabrication of transistor devices, and the resultant morphology of these networks are discussed in the next chapter. Standard photolithographic methods were used to successfully fabricate carbon nanotube and graphene field effect transistor devices. A range of photolithography types and electrode/encapsulation materials were trialled to find the optimal device composition for sensing, also discussed in the next chapter. Atomic force microscopy, fluorescence microscopy and a variety of electrical measurement setups were used to characterise the devices.



## 5. Characteristics of Pristine Carbon Nanotube & Graphene Field Effect Transistors

### 5.1. Carbon Nanotube Network Morphology

Figure 5.1 shows a side-by-side comparison of the surface morphology of carbon nanotube films fabricated using the methods described in Section 4.1. These images were collected using an atomic force microscope and processed in the manner described in Section 4.3. They each show bundles of carbon nanotubes with a range of diameters and lengths, with each bundle containing one or multiple nanotubes. As discussed in previous works using solvent-based deposition techniques for depositing carbon nanotubes, multi-tube bundles form due to mutual attraction between nanotubes [4], [5], [13]. The diameter range provided by the supplier for the individual carbon nanotubes used is 1.2-1.7 nm, while the length range is 0.3-5.0  $\mu\text{m}$  (Nanointegris). Figures Figure 5.1c and Figure 5.1d also show the presence of some non-nanotube contaminants on the substrate surface, which could be tiny amounts of residual photoresist. The presence of residual photoresist is discussed further in Section 6.4.1.

The distribution of the deposited carbon nanotubes was modelled to quantitatively understand the effect of the various methods used on the resulting network morphology. The diameter range of deposited single-walled carbon nanotubes can be modelled via a normal or Gaussian distribution [4], [14], [15]. However, when we extract and bin the height profiles from the AFM images in Figure 5.1, the histograms do not follow a normal distribution. The AFM histogram shape results from the  $\text{SiO}_2$  substrate and carbon nanotubes both exhibiting some roughness, which is partially due to surface contamination by atmospheric contaminants. In the case of the surfactant-deposited networks, residual surfactant may also contribute to surface roughness [15]. However, it has been shown that bare  $\text{SiO}_2$  substrate has a surface roughness which can also be modelled with a normal distribution, with a height range of approximately  $\pm 1$  nm about the mean, which we set as 0 nm [16]. Therefore, we can assume that a better model for the AFM histograms is a linear combination of normal distributions.

By using the analysis discussed in Section B.2

5. Characteristics of Pristine Carbon Nanotube & Graphene Field Effect Transistors

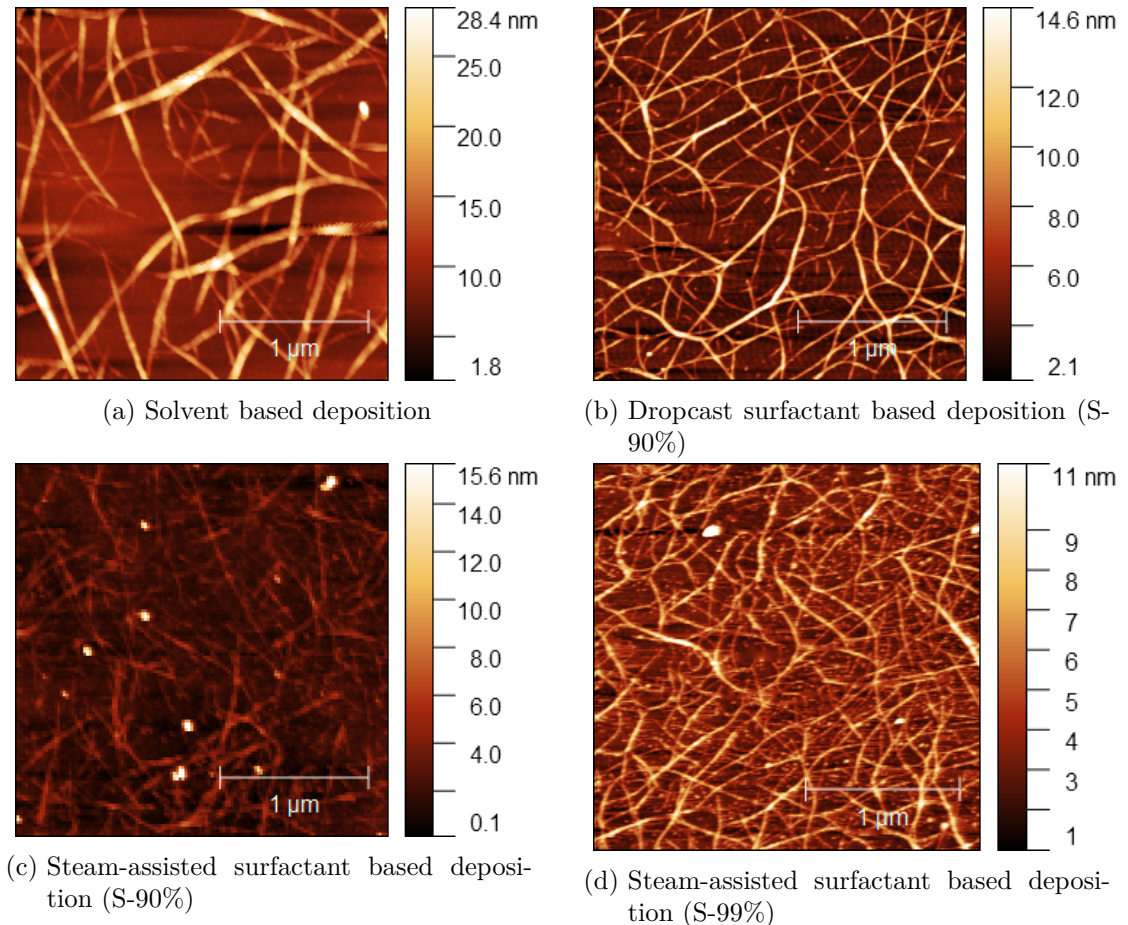


Figure 5.1.: Atomic force microscope images of carbon nanotube films deposited using various methods.

### 5.1. Carbon Nanotube Network Morphology

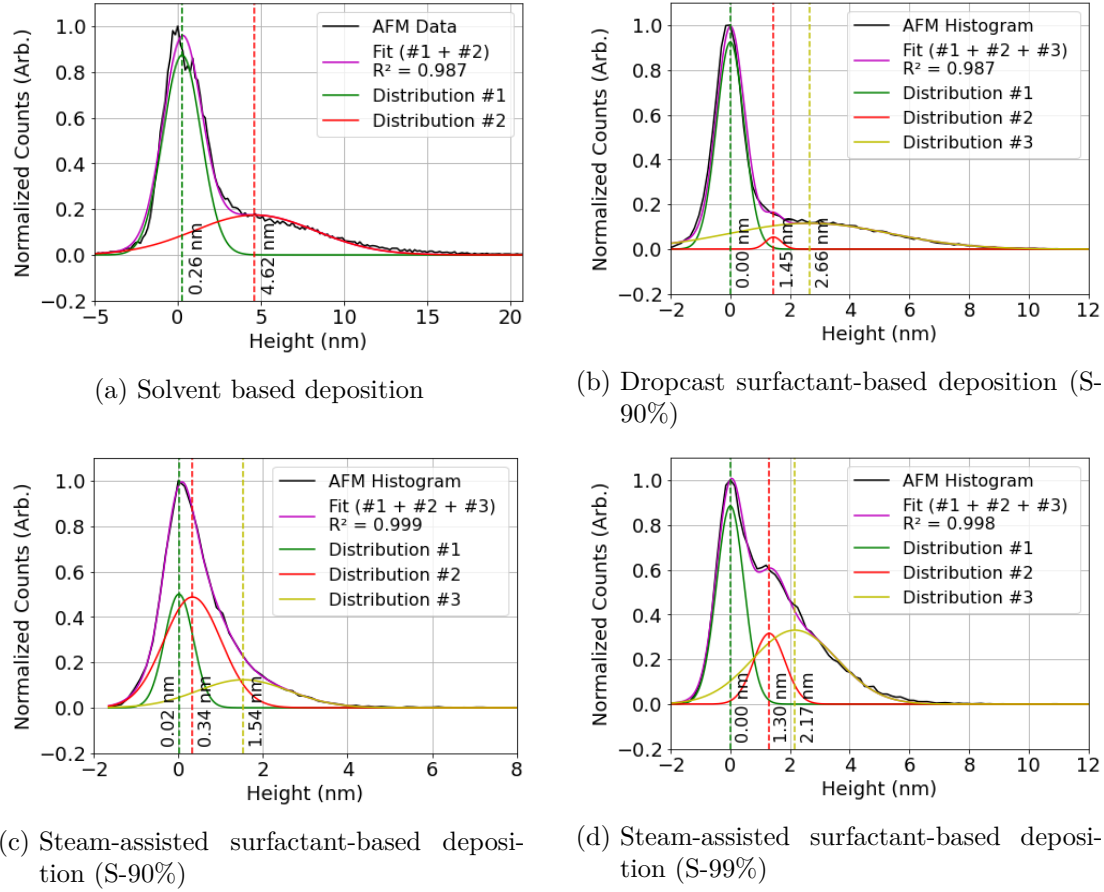


Figure 5.2.: Surface profile histograms extracted from the atomic force microscope images seen in Figure 5.1, each fitted with a linear combination of normal distributions. The component normal distributions corresponding to each linear combination are also shown.

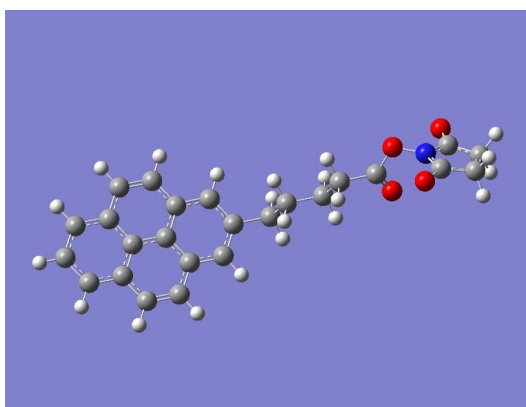
*5. Characteristics of Pristine Carbon Nanotube & Graphene Field Effect Transistors*

**5.2. Salt Concentration Sensing with Phosphate Buffered Saline**

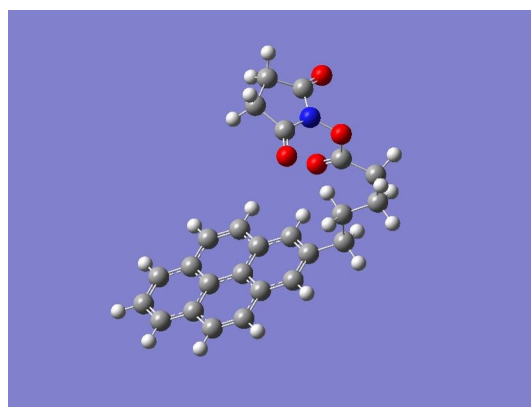
## 6. Functionalisation of Carbon Nanotubes and Graphene with Odorant Receptors

### 6.1. Linker molecules

#### 6.1.1. 1-Pyrenebutanoic acid N-hydroxysuccinimide ester (PBASE)



(a) Hartree-Fock energy: -3427728.67 kJ/mol  
(9 s.f.)



(b) Hartree-Fock energy: -3427729.66 kJ/mol  
(9 s.f.)

Figure 6.1.: Two conformations of PBASE molecule with geometry optimised via *ab initio* calculation (computed using Gaussian 16 [17]). The difference between computed Hartree-Fock energies is 1.0 kJ/mol, small enough that the existence of both molecular conformations is physically possible.

1-Pyrenebutanoic acid N-hydroxysuccinimide ester (variously known commercially and in the literature as 1-Pyrenebutyric acid N-hydroxysuccinimide ester, PBASE, PBSE, PASE, Pyr-NHS, PyBASE, PANHS) is a aromatic, bifunctional molecule commonly used for tethering biomolecules to the carbon rings of graphene and carbon nanotubes. The optimised molecular structure of PBASE is shown in Figure 6.1.

The non-covalent functionalisation of proteins onto a single-walled carbon nanotube using PBASE was first reported by Chen *et al.* in 2001 [18]. Two methods for protein functionalisation and immobilisation were successfully used, with the only differences being the solvent used to dissolve the PBASE powder (DMF, methanol) and the final

## *6. Functionalisation of Carbon Nanotubes and Graphene with Odorant Receptors*

concentration of the resulting solutions (6 mM, 1 mM respectively). The lower concentration may have been used for PBASE in methanol as PBASE powder appears to dissolve poorly in methanol at higher concentrations. Cella *et al.*, Campos *et al.*, Zheng *et al.* and Ohno *et al.* all directly cite Chen *et al.* when discussing functionalisation with PBASE [19]–[22]. Other groups using PBASE for graphene or carbon nanotube functionalisation do not explicitly reference Chen *et al.* in their methodology, but it is apparent they often draw on one of these two original methods. This common ancestry becomes apparent from the high frequency of methods detailing the use of 6 mM PBASE in DMF and 1 mM PBASE in methanol, as seen in Table 6.1.

However, despite this shared heritage, it is also apparent from Table 6.1 that there is a large degree of variation in the methods used for PBASE functionalisation. Various electrical characterisation, microscopy and spectroscopy techniques have been used to demonstrate successful functionalisation. However, there has historically been little justification provided for the exact parameters used in the procedure. As noted by Zhen *et al.* and Hinnemo *et al.*, there is more generally a lack of systematic research into formation of pyrene-derivative monolayers on graphene and other carbon nanomaterials, despite the wide use of this chemistry in the literature [23], [24].

We purchased PBASE from two suppliers, Sigma-Aldrich and Setareh Biotech. Sigma recommends DMF and methanol as suitable solvents for dissolving PBASE alongside chloroform and DMSO. Setareh Biotech indicates methanol can be used for dissolving PBASE. The two suppliers have conflicting information for suitable storage of PBASE, with Sigma recommending room temperature storage while Setareh Biotech recommends storage of  $-5$  to  $-30^{\circ}\text{C}$  and protection from light and moisture. Figure 6.2 compares the shapes of NMR spectra of PBASE from each supplier dissolved in DMSO, alongside a blank DMSO spectrum.

### 6.1. Linker molecules

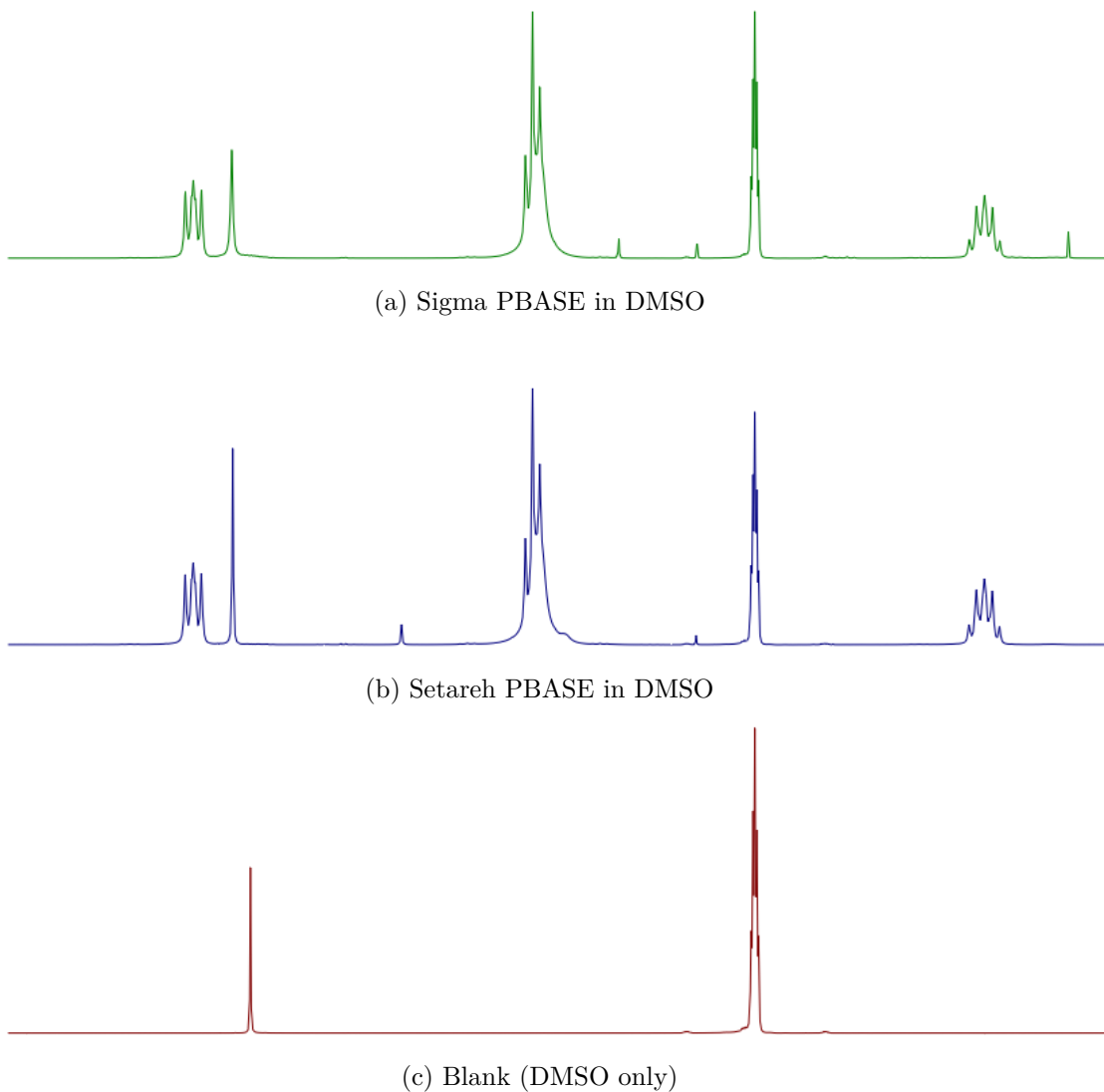


Figure 6.2.: Comparison of NMR spectrum profiles (arbitrary units)

## 6. Functionalisation of Carbon Nanotubes and Graphene with Odorant Receptors

Table 6.1.: Comparison of PBASE functionalisation processes used for immobilisation of proteins and aptamers onto liquid-gated CNTFET and graphene FET sensors

Solvent	Channel	Conc. (mM)	Incubation type	Time (hr)	Rinse steps	References
DMF	CNTs	5	Immersed	1	PBS	Maehashi <i>et al.</i> [25]
		6	Immersed	1	DMF, PBS	García-Aljaro <i>et al.</i> [26]
		6	Immersed	1	DMF	Chen <i>et al.</i> [18]
		6	Immersed	1	DMF	Cella <i>et al.</i> [19]
		6	Immersed	1	DMF	Das <i>et al.</i> [27]
	Graphene	-	-	2	DMF	Kwong Hong Tsang <i>et al.</i> [28]
		-	-	20	-	Wiedman <i>et al.</i> [29]
		0.2	Immersed	20	DMF, IPA, DI water	Gao <i>et al.</i> [30]
		1	100 $\mu$ L droplet	6	DMF, IPA, DI water	Nekrasov <i>et al.</i> [31]
		5	Immersed	1	DMF, DI water	Hwang <i>et al.</i> [32]
2-Methoxyethanol	Graphene	6	6 $\mu$ L droplet	2	DMF, DI water	Nur Nasufiya <i>et al.</i> [33]
		10	10 $\mu$ L droplet	2	DMF, DI water	Campos <i>et al.</i> [20]
		10	Immersed	2	DMF, PBS	Kuscu <i>et al.</i> [34]
		10	Immersed	1	DMF	Xu <i>et al.</i> [35]
		10	Immersed	12	DMF, ethanol, DI water	Khan <i>et al.</i> [36]
	CNTs	1	Immersed	1	DI water	Ono <i>et al.</i> [37]
		1	Immersed	1	Methanol, DI water	Zheng <i>et al.</i> [21]
		1	Immersed	2	Methanol	Kim <i>et al.</i> [38]
		5	Immersed	2	-	Sethi <i>et al.</i> [39]
		5	Immersed	1	Methanol, PBS	Ohno <i>et al.</i> [22]
DMSO	CNTs	10	-	1	DI water	Lopez <i>et al.</i> [40]
		10	Immersed	1	PBS	Strack <i>et al.</i> [41]

*6.2. Functionalisation with Odorant Receptors on CNT network*

**6.2. Functionalisation with Odorant Receptors on CNT network**

6.2.1. Varying CNT network fabrication approach

6.2.2. Varying OR-nanodisc preparation process

6.2.3. Varying solvent used

6.2.4. Other functionalisation approaches

**6.3. Functionalisation with Odorant Receptors on graphene**

**6.4. Verifying Pyrene Attachment to CNT network and graphene**

6.4.1. Photoresist contamination

6.4.2. Raman Spectroscopy

6.4.3. Pyrene-PEG-FITC fluorescence microscopy

Plasma clean comparison

Surfactant comparison

6.4.4. Pyrene-PEG electrical characterisation



# 7. Vapour Phase Sensing with Transistor Biosensors

## 7.1. Testing Vapour Delivery System

### 7.1.1. System Description

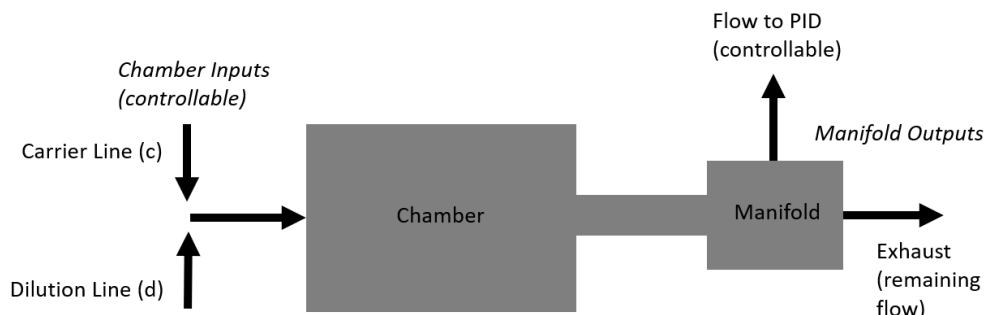


Figure 7.1.: Vapour Delivery System - Schematic of device chamber and manifold

### 7.1.2. Temperature and Humidity Indicator

### 7.1.3. Photoionisation Detector

#### Bubbling Vapour

First year report: ““First, a 200 sccm flow of N<sub>2</sub> gas was sent through the dilution line to the device chamber until 1000 s. Then, the flow controller three-way valves were manually adjusted so that the same 200 sccm flow was directed through 50 mL of EtOH analyte in the carrier line. This continued until 2200 s, where the valves were again manually adjusted so that 200 sccm clean N<sub>2</sub> again flowed through the device chamber. The resulting current across the device channel was monitored over this time, and is shown in Figure 19. A response to EtOH exposure and removal is visible.””



## 8. Summary

In summary, this book has no content whatsoever.

[1] 2



## A. Photolithography

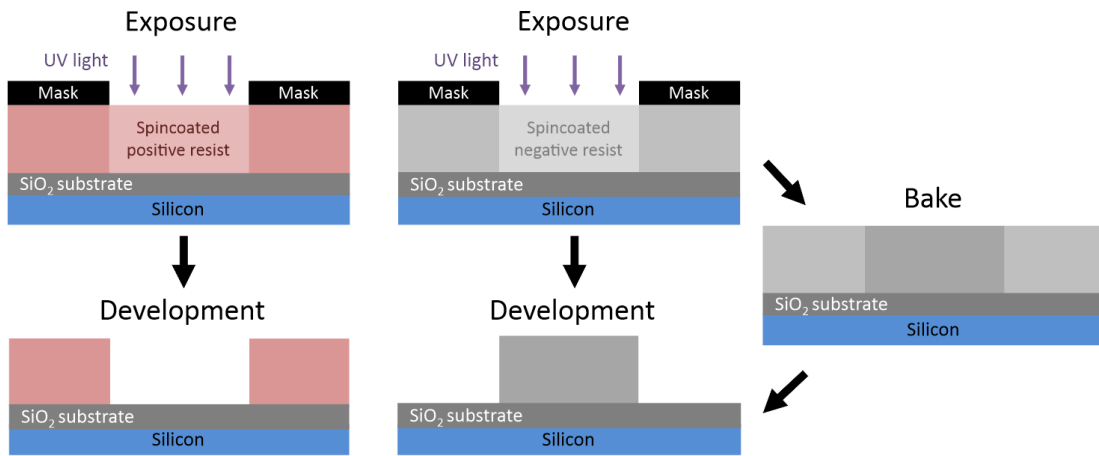


Figure A.1.: A side-view comparison of generic photolithography processes for positive and negative resists in the ideal case. Photolithography with a positive resist requires a single softbake step before exposure, while for negative resists a second baking step is required after exposure (Thicknesses shown not to scale).

This section details some of the standard photolithography procedures used in the device fabrication processes detailed in Chapter 4. Photoresists, also referred to here as “resists”, are UV light-sensitive polymeric resins used for photolithography. Both positive and negative photoresists were used in various fabrication processes. Positive resists are made soluble in alkalines by UV light exposure, meaning exposed areas are removed in the development process. Conversely, negative resists are cross-linked by exposure and a post-exposure bake step. The unexposed areas of the negative resist are then removed in the development process [42]. Figure A.1 gives a visual representation of these differences.

The specific photoresist selected for photolithography depends on the specific use case. The types used in this thesis are positive and negative AZ® photoresists (AZ® 1518, Microchemicals GmbH; AZ® nLOF 2020, Microchemicals GmbH) and SU-8 (SU8-2150, Kayaku Advanced Materials, formerly Microchem). The AZ® resists used here have a minimum film thickness of  $1.5 \mu\text{m}$  [42], while the SU8-2150 has a minimum film thickness of  $0.5 \mu\text{m}$  [43]. Positive resists which have not been thermally crosslinked will soften at higher temperatures ( $\gtrsim 100^\circ\text{C}$  for AZ® 1518), leading to a rounded profile. This is not

### *A. Photolithography*

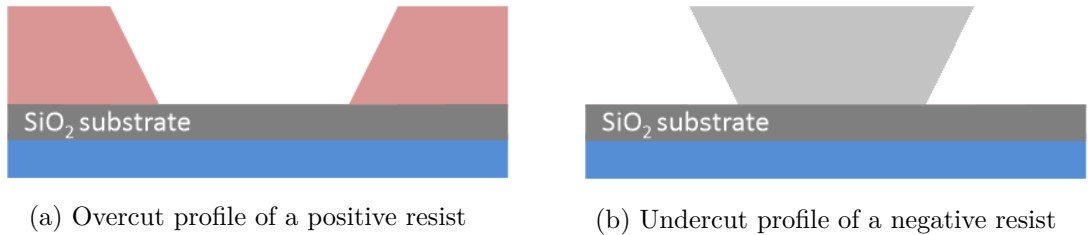


Figure A.2.: Two different resist profiles seen for different types of photoresist. Each profile has had the central region of the substrate exposed to UV light prior to development. The undercut profile is ideal for thin-film metal deposition and subsequent patterned removal, known as “lift-off”.

the case for negative resists, which are more thermally stable [42]. Each resist therefore has a different cross-section profile, as shown in Figure A.2.

If metal deposition is performed on a positive resist, some metal can collect on the outwardly-sloped sidewalls of the resist (see Figure A.2) which forms significant spikes on the edges of the deposited metal upon lift-off. On the other hand, metal cannot collect on top of the inwardly-sloped negative profile sidewalls, which avoids the formation of large edge spikes. Therefore, the negative resist profile is more suited to metal or metal oxide deposition and lift-off processes, though the process is more sensitive to human error due to requiring more processing steps than positive resist [42]. Finally, when it is suitably processed SU-8 is considered to be more stable and biocompatible than other photoresists [9]. It is especially biocompatible when chemically modified via processes such as isopropanol sonication and O<sub>2</sub> plasma treatment [8].

All photolithographic exposure was performed using a Karl Suss MJB3 Contact Aligner with a USHIO super-high pressure 350 W mercury lamp (USH-350DS, Japan). When performing photolithography, the intensity reading from the aligner was 20.8 - 24.2 mW/cm<sup>2</sup> (Note however that an external photometer reading at 400 nm found an intensity output of 17.2 mW/cm<sup>2</sup> when the aligner read 21.0 mW/cm<sup>2</sup>).

In general, photolithography procedures should be performed under yellow lighting, as light wavelengths from 320-450 nm can promote reactions in the photoresist used. Aging of photoresist over time can also significantly affect the photolithography process, and therefore all processes should be re-optimised regularly over time to give the desired result [42]. The range in processing times for some steps of the processes used here are largely due to the effects of aging on the photoresist.

The step-by-step processes for each resist are detailed in the subsequent sections.

## A.1. AZ® 1518 photoresist

1. Spincoat at a final speed of 4000 rotations per minute (rpm) for 1 minute, with an initial acceleration of 500 rpm/s (notes: clean the substrate with acetone, isopropanol (IPA) and nitrogen before spincoating; use only the minimum amount of photoresist required to fully cover the wafer surface; avoid any gaps or bubbles in the photoresist).
2. Softbake 2-4 minutes at 95°C on the hotplate (2 min for individual devices, 4 min for a quarter wafer)
3. Mask expose for 10-12 s (note: clean mask with acetone/IPA and N<sub>2</sub> dry before use)
4. Develop with 3 parts AZ® 326 (2.38 % TMAH metal-ion free developer, Microchemicals GmbH) in 1 part deionised (DI) water for 30-45 s (note: rinse for 10-15 s in one development solution, then perform the rest of the development in clean developer for a cleaner profile; lightly agitate the solution throughout the development process)
5. Rinse device for 30 s in DI water to remove excess developer, then dry under nitrogen

## A.2. AZ® nLOF 2020 photoresist

1. Spincoat at final speed of 3000 rotations per minute (rpm) for 1 minute, with an initial acceleration of 500 rpm/s (notes: clean the substrate with acetone, isopropanol (IPA) and nitrogen before spincoating; avoid any gaps or bubbles in the photoresist)
2. Softbake for precisely 60 s at 110°C on the hotplate
3. Mask expose for 2.7-3 s (note: clean mask with acetone/IPA and N<sub>2</sub> dry before use)
4. Post-exposure bake for precisely 60 s at 110°C on the hotplate to cross-link exposed resist
5. Develop with 3 parts AZ® 326 in 1 part DI water for 60-70 s (note: rinse for 30 s in one development solution, then perform the rest of the development in clean developer for a cleaner profile; lightly agitate the solution throughout the development process)
6. Rinse device for 30 s in DI water to remove excess developer, then dry under nitrogen

*A. Photolithography*

**A.3. SU8-2150 photoresist**

1. SU-8 was diluted in cyclopentanone until viscosity was low enough to spincoat on substrate and then sonicated at 50°C for 3-4 hours (Note: The dilution ratio used was ~1 part SU-8 to 5 parts cyclopentanone. However, the age of the SU-8 may mean that significant evaporation had occurred prior to use, and the amount of SU-8 actually present is underrepresented by this ratio)
2. Spincoat first with a final speed of 500 rpm (acceleration 500 rpm/s) for 10 seconds, followed by spincoating at 4000 rpm (acceleration 7500 rpm/s) for 40 s.
3. Softbake for 10 minutes at 95°C on the hotplate
4. Mask expose for 6-8 s (note: clean mask with acetone/IPA and N<sub>2</sub> dry before use)
5. Post-exposure bake for 10 minutes at 95°C on the hotplate to cross-link exposed resist
6. Develop with SU-8 developer (Kayaku Advanced Materials, formerly Microchem) for 10-15 s, then clean in IPA for 30 s, repeat this step once then dry under nitrogen (note: lightly agitate the solution throughout the development process)

## B. Python Code for Data Analysis

### B.1. Code Repository

The code used for general analysis of field-effect transistor devices in this thesis was written with Python 3.8.8. Contributors to the code used include Erica Cassie, Erica Happe, Marissa Dierkes and Leo Browning. The code is located on GitHub and the research group OneDrive, and is available on request.

### B.2. Atomic Force Microscope Histogram Analysis

The purpose of this code is to return morphology statistics such as height distribution and carbon nanotube coverage/density from atomic force microscope (AFM) images of carbon nanotube networks. The code uses the SciPy optimize package to fit two or three normal distributions to .xyz datasets from AFM images processed in Gwyddion (see Section 4.3). The number of normal distributions was chosen based on which gave a better quality fit to the .xyz data. It was originally designed by Erica Happe in Matlab, and adapted by Marissa Dierkes and myself for use in Python.

The .xyz data is initially sorted into bins with 0.15 nm size. The bin with the maximum number of counts is set at 0 nm, as this peak represents the mean of the surface roughness of the bare silicon. The fitting parameters  $m_1, s_1, k_1, m_2, s_2, k_2$  (as well as  $m_3, s_3, k_3$  for three normal distributions) are used in the objective function Equation B.1 when optimising.

$$f(x) = k_1 \exp\left(-\frac{(x - m_1)^2}{2s_1^2}\right) + k_2 \exp\left(-\frac{(x - m_2)^2}{2s_2^2}\right) + \dots \quad (\text{B.1})$$

These fitting parameters represent the mean (m), standard deviation (s) and amplitude (k) of each normal distribution. We can find the initial guess for these fitting parameters by using the histogram data to roughly approximate these values.  $k_1$  is taken as the maximum y-value of the data being fitted,  $m_1$  is set to zero and  $s_1$  is taken as one-third of the difference between  $m_1$  and the x-value of the first datapoint where the y-value is greater than 1% of  $k_1$ . We find the Gaussian given by these values, and subtract it from the existing dataset. We then take  $k_2$  to be the maximum y-value of this modified dataset, and  $m_1$  to be the x-value of the maximum y-value.  $s_2$  is taken as the difference

### B. Python Code for Data Analysis

between  $m_1$  and the x-value of the first datapoint where the y-value is greater than 60% of  $k_2$ . This process is repeated to find  $k_3$  and  $m_3$ , and  $s_3$  is one-third of the difference between  $m_3$  and the x-value of the *last* datapoint where the y-value is greater than 1% of  $k_3$ . In this iterative manner, we find a reasonably good initial guess for our fit.

Using the objective function with these fitting parameters in the `scipy.optimize.curve_fit` module, we receive optimised fitting parameters which gave an R-squared value of 0.98 or greater. By calculating the area under each of the normal distributions found from the fit, we can find the proportion of the surface covered by carbon nanotubes.

# C. Vapour Delivery System

## C.1. Technical Notes

Two LabView Virtual Instruments (VIs) were adapted from pre-existing VIs for operating the mass flow controllers and monitoring vapour flow into the device chamber, as well as monitoring temperature and humidity in the vapour delivery system's manifold. These VIs were named “ ” A third VI was developed in parallel which combined the first two Virtual Instruments, alongside allowing the sequence of values to control the mass flow controllers.

From Honours report: “ ” Figure 12 gives the right side of the front panel of the LabView VI sample with `vapour.VI`, which lets us preset an autonomously-performed vapour sensing sequence. Each row in each array module corresponds to a different step in this sequence. The ‘`howManySteps`’ module lets us set how many of these steps are performed. The ‘`Durations Array`’ module determines the length of time in seconds each step is performed over. The ‘`Carrier Flows Array`’ and ‘`Dilution Flows Array`’ modules let us set the carrier flow and dilution flow, respectively, in standard cubic centimetres per minute (sccm) through the gas rig at each step. The carrier flow pushes analyte vapour into the vapour-sensing device chamber, while dilution flow is used to modify the flow behaviour of the analyte vapour entering the chamber. The vapour sensing sequence as depicted in Figure 12 was used for all vapour sensing runs in this investigation. At the end of the sequence, the data collected about the vapour sensing process was saved as an `.lvm` file. “ ”

## C.2. Future Improvements



# Bibliography

- [1] Jisook Oh, Jihyun Myoung, Jin Sung Bae, et al. “Etch Behavior of ALD Al<sub>2</sub>O<sub>3</sub> on HfSiO and HfSiON Stacks in Acidic and Basic Etchants”. In: *Journal of The Electrochemical Society* 158.4 (Apr. 2011), pp. D217–D222. ISSN: 0013-4651. DOI: 10.1149/1.3554729/XML. URL: <https://iopscience.iop.org/article/10.1149/1.3554729>.  
https://iopscience.iop.org/article/10.1149/1.3554729/meta.
- [2] Muhammad Munem Ali, Jacob John Mitchell, Gregory Burwell, et al. “Application of Molecular Vapour Deposited Al<sub>2</sub>O<sub>3</sub> for Graphene-Based Biosensor Passivation and Improvements in Graphene Device Homogeneity”. In: *Nanomaterials* 11.8 (Aug. 2021). ISSN: 20794991. DOI: 10.3390/NANO11082121. URL: /pmc/articles/PMC8398646/%20/pmc/articles/PMC8398646/?report=abstract%20https://www.ncbi.nlm.nih.gov/pmc/articles/PMC8398646/.
- [3] Vittorio Guarneri, Leonardo Biazi, Roberto Marchiori, et al. “Platinum metallization for MEMS application. Focus on coating adhesion for biomedical applications”. In: *Biomatter* 4.1 (Jan. 2014), e28822. ISSN: 2159-2535. DOI: 10.4161/Biom.28822. URL: <https://pubmed.ncbi.nlm.nih.gov/24743057/>.
- [4] Murugathas Thanihaichelvan, Leo A. Browning, Marissa P. Dierkes, et al. “Data on liquid gated CNT network FETs on flexible substrates”. In: *Data in Brief* 21 (Dec. 2018), pp. 276–283. ISSN: 2352-3409. DOI: 10.1016/J.DIB.2018.09.093.
- [5] Murugathas Thanihaichelvan, Leo A. Browning, Marissa P. Dierkes, et al. “Metallic-semiconducting junctions create sensing hot-spots in carbon nanotube FET aptasensors near percolation”. In: *Biosensors and Bioelectronics* 130 (Apr. 2019), pp. 408–413. ISSN: 0956-5663. DOI: 10.1016/J.BIOS.2018.09.021.
- [6] Bajramshahe Shkodra, Mattia Petrelli, Martina Aurora Costa Angeli, et al. “Electrolyte-gated carbon nanotube field-effect transistor-based biosensors: Principles and applications”. In: *Applied Physics Reviews* 8.4 (Dec. 2021), p. 41325. ISSN: 19319401. DOI: 10.1063/5.0058591/1076095. URL: /aip/apr/article/8/4/041325/1076095/Electrolyte-gated-carbon-nanotube-field-effect.
- [7] Chang Young Lee, Seunghyun Balk, Jianqi Zhang, et al. “Charge transfer from metallic single-walled carbon nanotube sensor arrays”. In: *Journal of Physical Chemistry B* 110.23 (June 2006), pp. 11055–11061. ISSN: 15206106. DOI: 10.1021/JP056425V/SUPPL\_FILE/JP056425VSI20060322\_123713.PDF. URL: <http://pubs.acs.org/doi/full/10.1021/jp056425v>.

## Bibliography

- [8] Ziyu Chen and Jeong Bong Lee. “Biocompatibility of SU-8 and Its Biomedical Device Applications”. In: *Micromachines* 2021, Vol. 12, Page 794 12.7 (July 2021), p. 794. ISSN: 2072-666X. DOI: 10.3390/MI12070794. URL: <https://www.mdpi.com/2072-666X/12/7/794>.
- [9] Faris M. Albarghouthi, Nicholas X. Williams, James L. Doherty, et al. “Passivation Strategies for Enhancing Solution-Gated Carbon Nanotube Field-Effect Transistor Biosensing Performance and Stability in Ionic Solutions”. In: *ACS Applied Nano Materials* 5.10 (Oct. 2022), pp. 15865–15874. ISSN: 25740970. DOI: 10.1021/ACS ANM.2C04098/SUPPL\_FILE/AN2C04098\_SI\_001.PDF. URL: <https://doi.org/10.1021/acsanm.2c04098>.
- [10] James Kolodzey, Enam Ahmed Chowdhury, Thomas N Adam, et al. “Electrical Conduction and Dielectric Breakdown in Aluminum Oxide Insulators on Silicon”. In: *IEEE TRANSACTIONS ON ELECTRON DEVICES* 47.1 (2000), p. 121.
- [11] Kenneth R. Spring and Michael W. Davidson. *Introduction to Fluorescence Microscopy / Nikon’s MicroscopyU*. URL: <https://www.microscopyu.com/techniques/fluorescence/introduction-to-fluorescence-microscopy> (visited on 2023-08-18).
- [12] Rudi Rottenfusser, Erin E. Wilson, and Michael W. Davidson. *ZEISS Microscopy Online Campus / Microscopy Basics / Fluorescence Microscopy*. URL: <https://zeiss-campus.magnet.fsu.edu/articles/basics/fluorescence.html> (visited on 2023-08-18).
- [13] H. Y. Zheng and N. O.V. Plank. “Facile fabrication of carbon nanotube network thin film transistors for device platforms”. In: *International Journal of Nanotechnology* 14.1-6 (2017), pp. 505–518. ISSN: 14757435. DOI: 10.1504/IJNT.2017.082473.
- [14] Chang Liu and Hui Ming Cheng. “Carbon nanotubes: controlled growth and application”. In: *Materials Today* 16.1-2 (Jan. 2013), pp. 19–28. ISSN: 1369-7021. DOI: 10.1016/J.MATTOD.2013.01.019.
- [15] Dusan Vobornik, Maohui Chen, Shan Zou, et al. “Measuring the Diameter of Single-Wall Carbon Nanotubes Using AFM”. In: *Nanomaterials* 13.3 (Feb. 2023), p. 477. ISSN: 20794991. DOI: 10.3390/NANO13030477/S1. URL: <https://www.mdpi.com/2079-4991/13/3/477>.
- [16] Matěj Velický, Adam J Cooper, Peter S Toth, et al. “Mechanical stability of substrate-bound graphene in contact with aqueous solutions”. In: *2D Materials* 2.2 (May 2015), p. 024011. ISSN: 2053-1583. DOI: 10.1088/2053-1583/2/2/024011. URL: <https://iopscience.iop.org/article/10.1088/2053-1583/2/2/024011%20https://iopscience.iop.org/article/10.1088/2053-1583/2/2/024011/meta>.
- [17] J. A. M. J. Frisch and G. W. Trucks and H. B. Schlegel and G. E. Scuseria and M. A. Robb and J. R. Cheeseman and G. Scalmani and V. Barone and G. A. Petersson and H. Nakatsuji and X. Li and M. Caricato and A. V. Marenich and J. Bloino and B. G. Janesko and R. G, J. E. Peralta, F. Ogliaro, et al. *Gaussian~16 Revision C.01*. 2016.

- [18] R. J. Chen, Y. Zhang, D. Wang, et al. “Noncovalent sidewall functionalization of single-walled carbon nanotubes for protein immobilization”. In: *Journal of the American Chemical Society* 123.16 (2001), pp. 3838–3839. ISSN: 00027863. DOI: 10.1021/ja010172b. URL: <http://pubs.acs.org..>
- [19] Lakshmi N. Cella, Pablo Sanchez, Wenwan Zhong, et al. “Nano aptasensor for Protective Antigen Toxin of Anthrax”. In: *Analytical Chemistry* 82.5 (Mar. 2010), pp. 2042–2047. ISSN: 00032700. DOI: 10.1021/ac902791q. URL: <https://pubs.acs.org/doi/full/10.1021/ac902791q>.
- [20] Rui Campos, Jérôme Borme, Joana Rafaela Guerreiro, et al. “Attomolar label-free detection of dna hybridization with electrolyte-gated graphene field-effect transistors”. In: *ACS Sensors* 4.2 (Feb. 2019), pp. 286–293. ISSN: 23793694. DOI: 10.1021/acssensors.8b00344. URL: <https://pubs.acs.org/doi/full/10.1021/acssensors.8b00344>.
- [21] Han Yue Zheng, Omar A. Alsager, Bicheng Zhu, et al. “Electrostatic gating in carbon nanotube aptasensors”. In: *Nanoscale* 8.28 (July 2016), pp. 13659–13668. ISSN: 20403372. DOI: 10.1039/c5nr08117c. URL: <https://pubs.rsc.org/en/content/articlehtml/2016/nr/c5nr08117c%20https://pubs.rsc.org/en/content/articlelanding/2016/nr/c5nr08117c>.
- [22] Yasuhide Ohno, Kenzo Maehashi, and Kazuhiko Matsumoto. “Label-free biosensors based on aptamer-modified graphene field-effect transistors”. In: *Journal of the American Chemical Society* 132.51 (Dec. 2010), pp. 18012–18013. ISSN: 00027863. DOI: 10.1021/ja108127r. URL: <https://pubs.acs.org/doi/full/10.1021/ja108127r>.
- [23] Xue V. Zhen, Emily G. Swanson, Justin T. Nelson, et al. “Noncovalent monolayer modification of graphene using pyrene and cyclodextrin receptors for chemical sensing”. In: *ACS Applied Nano Materials* 1.6 (June 2018), pp. 2718–2726. ISSN: 25740970. DOI: 10.1021/ACSANM.8B00420/ASSET/IMAGES/LARGE/AN-2018-00420J\_0004.jpeg. URL: <https://pubs.acs.org/doi/full/10.1021/acsanm.8b00420>.
- [24] Malcolm Hinnemo, Jie Zhao, Patrik Ahlberg, et al. “On Monolayer Formation of Pyrenebutyric Acid on Graphene”. In: *Langmuir* 33.15 (Apr. 2017), pp. 3588–3593. ISSN: 15205827. DOI: 10.1021/ACS.LANGMUIR.6B04237/ASSET/IMAGES/LARGE/LA-2016-04237V\_0003.jpeg. URL: <https://pubs.acs.org/doi/full/10.1021/acs.langmuir.6b04237>.
- [25] Kenzo Maehashi, Taiji Katsura, Kagan Kerman, et al. “Label-free protein biosensor based on aptamer-modified carbon nanotube field-effect transistors”. In: *Analytical Chemistry* 79.2 (Jan. 2007), pp. 782–787. ISSN: 00032700. DOI: 10.1021/ac060830g. URL: <https://pubs.acs.org/doi/full/10.1021/ac060830g>.
- [26] Cristina García-Aljaro, Lakshmi N. Cella, Dhamanand J. Shirale, et al. “Carbon nanotubes-based chemiresistive biosensors for detection of microorganisms”. In: *Biosensors and Bioelectronics* 26.4 (Dec. 2010), pp. 1437–1441. ISSN: 09565663. DOI: 10.1016/j.bios.2010.07.077.

## Bibliography

- [27] Basanta K. Das, Chaker Tlili, Sushmee Badhulika, et al. “Single-walled carbon nanotubes chemiresistor aptasensors for small molecules: Picomolar level detection of adenosine triphosphate”. In: *Chemical Communications* 47.13 (Mar. 2011), pp. 3793–3795. ISSN: 1364548X. DOI: 10.1039/c0cc04733c. URL: <https://pubs.rsc.org/en/content/articlehtml/2011/cc/c0cc04733c%20https://pubs.rsc.org/en/content/articlelanding/2011/cc/c0cc04733c>.
- [28] Deana Kwong Hong Tsang, Tyler J. Lieberthal, Clare Watts, et al. “Chemically Functionalised Graphene FET Biosensor for the Label-free Sensing of Exosomes”. In: *Scientific Reports* 9.1 (Sept. 2019), pp. 1–10. ISSN: 20452322. DOI: 10.1038/s41598-019-50412-9. URL: <https://www.nature.com/articles/s41598-019-50412-9>.
- [29] Gregory R. Wiedman, Yanan Zhao, Arkady Mustaev, et al. “An Aptamer-Based Biosensor for the Azole Class of Antifungal Drugs”. In: *mSphere* 2.4 (Aug. 2017). ISSN: 23795042. DOI: 10.1128/msphere.00274-17. URL: [/pmc/articles/PMC5566834](https://pmc/articles/PMC5566834/)?report=abstract%20https://www.ncbi.nlm.nih.gov/pmc/articles/PMC5566834/
- [30] Zhaoli Gao, Han Xia, Jonathan Zauberman, et al. “Detection of Sub-fM DNA with Target Recycling and Self-Assembly Amplification on Graphene Field-Effect Biosensors”. In: *Nano Letters* 18.6 (June 2018), pp. 3509–3515. ISSN: 15306992. DOI: 10.1021/acs.nanolett.8b00572. URL: <https://pubs.acs.org/doi/full/10.1021/acs.nanolett.8b00572>.
- [31] Nikita Nekrasov, Natalya Yakunina, Averyan V. Pushkarev, et al. “Spectral-phase interferometry detection of ochratoxin a via aptamer-functionalized graphene coated glass”. In: *Nanomaterials* 11.1 (Jan. 2021), pp. 1–10. ISSN: 20794991. DOI: 10.3390/nano11010226. URL: <https://www.mdpi.com/2079-4991/11/1/226>%20https://www.mdpi.com/2079-4991/11/1/226.
- [32] Michael T. Hwang, B. Landon Preston, Lee Joon, et al. “Highly specific SNP detection using 2D graphene electronics and DNA strand displacement”. In: *Proceedings of the National Academy of Sciences of the United States of America* 113.26 (June 2016), pp. 7088–7093. ISSN: 10916490. DOI: 10.1073/pnas.1603753113. URL: <https://www.pnas.org/doi/abs/10.1073/pnas.1603753113>.
- [33] Mohd Maidin Nur Nasyifa, A. Rahim Ruslinda, Nur Hamidah Abdul Halim, et al. “Immuno-probed graphene nanoplatelets on electrolyte-gated field-effect transistor for stable cortisol quantification in serum”. In: *Journal of the Taiwan Institute of Chemical Engineers* 117 (Dec. 2020), pp. 10–18. ISSN: 18761070. DOI: 10.1016/j.jtice.2020.12.008.
- [34] Murat Kuscu, Hamideh Ramezani, Ergin Dinc, et al. “Graphene-based Nanoscale Molecular Communication Receiver: Fabrication and Microfluidic Analysis”. In: (June 2020). arXiv: 2006.15470. URL: <https://arxiv.org/abs/2006.15470v2>.

## Bibliography

- [35] Shicai Xu, Jian Zhan, Baoyuan Man, et al. “Real-time reliable determination of binding kinetics of DNA hybridization using a multi-channel graphene biosensor”. In: *Nature Communications* 8.1 (Mar. 2017), pp. 1–10. ISSN: 20411723. DOI: 10.1038/ncomms14902. URL: <https://www.nature.com/articles/ncomms14902>.
- [36] Niazul I. Khan, Mohammad Mousazadehkasin, Sujoy Ghosh, et al. “An integrated microfluidic platform for selective and real-time detection of thrombin biomarkers using a graphene FET”. In: *Analyst* 145.13 (June 2020), pp. 4494–4503. ISSN: 13645528. DOI: 10.1039/d0an00251h. URL: <https://pubs.rsc.org/en/content/articlehtml/2020/an/d0an00251h%20https://pubs.rsc.org/en/content/articlelanding/2020/an/d0an00251h>.
- [37] T Ono, K Kamada, R Hayashi, et al. “Lab-on-a-graphene-FET detection of key molecular events underpinning influenza 2 virus infection and effect of antiviral drugs 3 Running title: Graphene-FET detects reactions in an influenza infection MAIN TEXT”. In: *bioRxiv* (Mar. 2020), p. 2020.03.18.996884. DOI: 10.1101/2020.03.18.996884. URL: <https://doi.org/10.1101/2020.03.18.996884>.
- [38] Jun Pyo Kim, Byung Yang Lee, Joohyung Lee, et al. “Enhancement of sensitivity and specificity by surface modification of carbon nanotubes in diagnosis of prostate cancer based on carbon nanotube field effect transistors”. In: *Biosensors and Bioelectronics* 24.11 (July 2009), pp. 3372–3378. ISSN: 09565663. DOI: 10.1016/j.bios.2009.04.048. URL: <https://pubmed.ncbi.nlm.nih.gov/19481922/>.
- [39] Jagriti Sethi, Michiel Van Bulck, Ahmed Suhail, et al. “A label-free biosensor based on graphene and reduced graphene oxide dual-layer for electrochemical determination of beta-amyloid biomarkers”. In: *Microchimica Acta* 187.5 (May 2020), pp. 1–10. ISSN: 14365073. DOI: 10.1007/s00604-020-04267-x. URL: <https://link.springer.com/article/10.1007/s00604-020-04267-x>.
- [40] Ryan J. Lopez, Sofia Babanova, Kateryna Artyushkova, et al. “Surface modifications for enhanced enzyme immobilization and improved electron transfer of PQQ-dependent glucose dehydrogenase anodes”. In: *Bioelectrochemistry* 105 (Oct. 2015), pp. 78–87. ISSN: 1878562X. DOI: 10.1016/j.bioelechem.2015.05.010. URL: <https://pubmed.ncbi.nlm.nih.gov/26011132/>.
- [41] Guinevere Strack, Robert Nichols, Plamen Atanassov, et al. “Modification of carbon nanotube electrodes with 1-pyrenebutanoic acid, succinimidyl ester for enhanced bioelectrocatalysis”. In: *Methods in Molecular Biology* 1051 (2013), pp. 217–228. ISSN: 10643745. DOI: 10.1007/978-1-62703-550-7\_14. URL: <https://pubmed.ncbi.nlm.nih.gov/23934807/>.
- [42] MicroChemicals. *Photoresists AZ and MicroChemicals TI resists*. URL: <https://www.microchemicals.com/products/photoresists.html> (visited on 2023-06-09).
- [43] Kayaku (Microchem). *SU-8 2000 Permanent Negative Epoxy Photoresist / Kayaku*. URL: <https://kayakuam.com/products/su-8-2000/> (visited on 2023-06-30).